ADVANCED MATERIALS
www.advmat.de

Multiphase Morphology with Enhanced Carrier Lifetime via Quaternary Strategy Enables High-Efficiency, Thick-Film, and Large-Area Organic Photovoltaics

Lingling Zhan, Shouchun Yin,* Yaokai Li, Shuixing Li, Tianyi Chen, Rui Sun, Jie Min, Guanqing Zhou, Haiming Zhu, Yiyao Chen, Jin Fang, Chang-Qi Ma, Xinxin Xia, Xinhui Lu, Huayu Qiu, Weifei Fu,* and Hongzheng Chen**

With the continuous breakthrough of the efficiency of organic photovoltaics (OPVs), their practical applications are on the agenda. However, the thickness tolerance and upscaling in recently reported high-efficiency devices remains challenging. In this work, the multiphase morphology and desired carrier behaviors are realized by utilizing a quaternary strategy. Notably, the exciton separation, carrier mobility, and carrier lifetime are enhanced significantly, the carrier recombination and the energy loss (E_{loss}) are reduced, thus beneficial for a higher short-circuit density (J_{SC}), fill factor (FF), and open-circuit voltage (V_{OC}) of the quaternary system. Moreover, the intermixing-phase size is optimized, which is favorable for constructing the thick-film and large-area devices. Finally, the device with a 110 nm-thick active layer shows an outstanding power conversion efficiency (PCE) of 19.32% (certified 19.35%). Furthermore, the large-area (1.05 and 72.25 cm^2) devices with 110 nm thickness present PCEs of 18.25% and 12.20%, and the device with a 305 nm-thick film (0.0473 cm^2) delivers a PCE of 17.55%, which are among the highest values reported. The work demonstrates the potential of the quaternary strategy for large-area and thick-film OPVs and promotes the practical application of OPVs in the future.

1. Introduction

Organic photovoltaics (OPVs) as the efficient clean energy devices have unique advantages, such as low cost, lightweight, solution processability, semitransparent, etc., which make them have great potential in applications of smart windows and flexible wearable devices.[1–5] With the advanced high-efficiency materials and device engineering,[6–11] the power conversion efficiency (PCE) of single-junction OPV has exceeded 19%.[10,12–15] However, state-of-the-art high-efficiency OPVs are based on an active layer thickness of ≈100 nm and a small device area (≈0.05 cm^2).[16–18]

In the OPV system, increasing the thickness of the active layer will usually cause severe charge recombination due to low carrier mobility. Furthermore,

---

L. Zhan, S. Yin, H. Qiu
Key Laboratory of Organosilicon Chemistry and Materials Technology of Ministry of Education
College of Material
Chemistry and Chemical Engineering
Hangzhou Normal University
Hangzhou 311121, P. R. China
E-mail: linglingzhan@hznu.edu.cn; yinsc@hznu.edu.cn

L. Zhan, Y. Li, S. Li, T. Chen, W. Fu, H. Chen
State Key Laboratory of Silicon Materials
MOE Key Laboratory of Macromolecular Synthesis and Functionalization
International Research Center for X Polymers
Department of Polymer Science and Engineering
Zhejiang University
Hangzhou 310027, P. R. China
E-mail: linglingzhan@hznu.edu.cn; wffu@uw.edu; hzchen@zju.edu.cn

R. Sun, J. Min
The Institute for Advanced Studies
Wuhan University
Wuhan 430072, P. R. China

G. Zhou, H. Zhu
Department of Chemistry
Zhejiang University
Hangzhou 310027, P. R. China

Y. Chen
Vacuum Interconnected Nanotech Workstation (Nano-X)
Suzhou Institute of Nano-Tech and Nano-Bionics
Chinese Academy of Sciences (CAS)
Suzhou 215123, P. R. China

J. Fang, C.-Q. Ma
i-Lab & Printable Electronics Research Centre
Suzhou Institute of Nano-Tech and Nano-Bionics
Chinese Academy of Sciences (CAS)
Suzhou 215123, P. R. China

X. Xia, X. Lu
Department of Physics
Chinese University of Hong Kong
New Territories, Hong Kong 999077, P. R. China

The ORCID identification number(s) for the author(s) of this article can be found under https://doi.org/10.1002/adma.202206269.

DOI: 10.1002/adma.202206269

the thicker and larger films processed by blade-coating or slot-die coating will endure a more prolonged phase evolution time during solvent evaporation for phase transition, and the phase-separation size will be further amplified, resulting in a dramatic drop in efficiency for thick-film and large-area devices.[19–21] Therefore, the efficiency reduction caused by the sensitivity of active layer thickness and device area significantly limits the commercialization of OPVs. Developing high-performance OPVs with high tolerance to film thickness variation is highly appreciable for the high-throughput R2R processing.[22] Surprisingly, the Y-series nonfullerene acceptor (NFA) exhibits long exciton diffusion length, increasing active-layer thickness tolerance.[23–25] If the carrier lifetime and mobility of the Y-system are further improved, and the phase separation size can be finer controlled, thick-film and large-area devices can be achieved.

The behavior of carriers in OPV system is significantly affected by the morphology of the active layer.[26–29] Many efforts have been made to improve the carrier mobilities. For example, the third component in a ternary OPV with a parallel-like phase morphology is located at the host donor/acceptor interface, which could generate additional charge transport channels, facilitating exciton dissociation and carrier transportation.[30] An alloy-like phase morphology will be formed by adding a third component which has good compatibility with the original acceptor. The phase purity of the donor and the crystallinity of this system will be improved to realize increased carrier mobility and high-performance thick-film OPVs.[31] Both the alloy-like phase and the parallel-like phase are favorable for carrier behaviors and can be achieved via a ternary strategy.[32] However, the coexistence of multiphase morphology in one blend seems to be a challenge. The multicomponent strategy was proved to be an effective method for morphology regulation.[33–35] Liu et al. constructed a quaternary blend by choosing two donors with cascade energy levels, and paired them with fullerene acceptor (FA) and NFA, $PC_{71}BM$, and Y6.[36] The multicomponent blend demonstrates double-cascade charge transport channels for high-performance. Yan et al. achieved a "Rivers and Streams"-type hierarchical morphology through a suitable combination of donors and acceptors (including FA), achieving quaternary OPVs with outstanding performance.[35] FAs have advantages of good compatibility and high mobility and are good choices as the fourth component. However, FAs show limited contributions to the photocurrent due to the wide bandgap.[37–40] Thus, constructing a quaternary system with all-NFAs is promising to achieve a breakthrough in performance of OPVs.

Herein, we adopt a fullerene-free quaternary strategy for morphology regulation and carrier behavior optimization, and high-performance devices with thick active layers and large-area were achieved. High-efficiency donor PM6 and Y-series acceptors, L8-BO and BTP-eC9 are used as the host parts of the quaternary system, and the asymmetric acceptor BTP-S10 with low energy loss developed by our group is used as the fourth component. Through simple contact angle testing and wetting coefficient calculation, we found that mixing BTP-eC9 and L8-BO at a ratio of 1:1 with PM6 could form the interfacial location of BTP-eC9 and L8-BO, thereby realizing the parallel-like phase in PM6:BTP-eC9:L8-BO blend. BTP-eC9 and BTP-S10 can form an alloy-like phase and improve the phase purity of PM6 in the quaternary blend. Thus, we obtain a quaternary system with a multiphase distribution through optimization. The quaternary device exhibits a more suitable phase separation size, efficient exciton dissociation, improved hole mobility, enhanced carrier lifetime, and reduced charge recombination. These features facilitate the realization of thick-film and large-area devices. Finally, the quaternary device (0.0473 cm^2, 110 nm) can achieve a high efficiency of 19.32% (certified 19.35%). The 1.05 and 72.25 cm^2 large-area devices (110 nm) can realize outstanding PCEs of 18.2% and 12.2%, and the device (0.0473 cm^2) with a 305 nm-thick active layer can achieve a high PCE of 17.55%, which are among the highest values for the reported large-area devices and thick-film devices so far. Our work provides a convenient method to construct a quaternary OPV with multiphase morphology and preferable carrier dynamics.

2. Results and Discussion

2.1. Multiphase Morphology Analysis

Figure 1a shows the chemical structures of polymer donor PM6, NFAs BTP-eC9, and L8-BO, and asymmetric NFA BTP-S10. BTP-eC9 and L8-BO are efficient NFAs with the same terminal group for ordered molecular packing and the differences in alkyl side chains on the center-core are for morphology regulation.[41,42] Both BTP-eC9 and L8-BO show high crystallinity and thus lead to an oversized separated phase in the mixture blend, which are unsuitable for thick-film devices. Besides, the open-circuit voltage (V_{OC}) is limited due to the obvious energy loss (E_{loss}) of PM6:BTP-eC9:L8-BO. Based on the above considerations, BTP-S10 with low E_{loss} is the suitable fourth component candidate due to its poor miscibility with PM6 and good compatibility with BTP-eC9, which is beneficial for the more delicate morphology modulation of the quaternary blend. The quaternary materials with various miscibilities show complementary absorption (Figure 1b) and suitable energy level distribution (Figure 1c), and the multiphase coexistence could be expected for desired carrier behavior.

To check the miscibility and the multiphase morphology of the quaternary blend, contact angle testing (**Figure 2**a and Table S1, Supporting Information) was performed. The Flory–Huggins interaction parameter χ presents the miscibility between two materials.[43] The value of $\chi^{D\text{-}A}$ between the donor (PM6) and acceptors (BTP-eC9, L8-BO, and BTP-S10) is calculated as 0.86, 0.46, and 2.12, respectively. Larger $\chi^{D\text{-}A}$ indicates the worse miscibility.[44] The various miscibility of quaternary combinations provide opportunities for the existence of multiphases.

The wetting coefficient $\left(\omega, \omega_{A_2} = \left(\gamma_{A_1/A_2} - \gamma_{D/A_2}\right)/\gamma_{D/A_1}\right)$ of the additional component in the host blend was calculated, which could infer the location of the added component in the ternary or quaternary blend. For the PM6:BTP-eC9:L8-BO blend, the $\omega_{L8\text{-}BO}$ is calculated as -0.70 (the third acceptor (A_2) will infuse into the phase of host acceptor (A_1) if the wetting coefficient is smaller than -1, while into the domain of host donor (D) if ω_{A_2} is larger than 1, and if $-1 < \omega_{A_2} < 1$, then A_2 will be located at the interfaces of D and A_1) , [45] indicating that L8-BO is located at the interfaces of PM6 and BTP-eC9, which is preferred to the

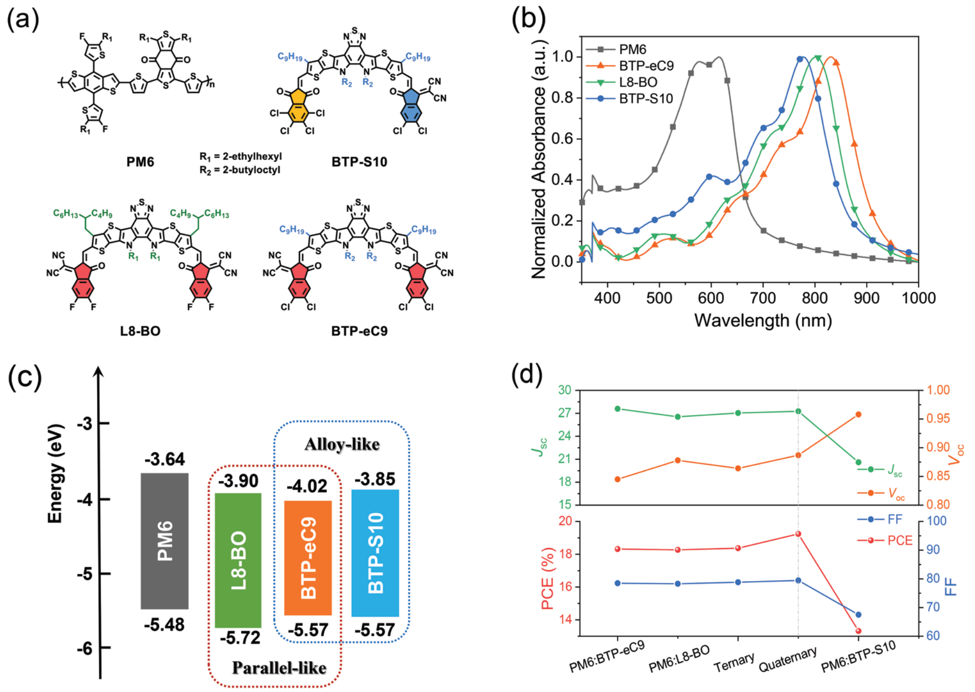

Figure 1. a) Chemical structures of PM6, BTP-eC9, L8-BO, and BTP-S10. b) Normalized UV–vis spectra of neat films. c) Energy diagram of PM6, BTP-eC9, L8-BO, and BTP-S10 determined by CV measurements. d) J_{SC}, V_{OC}, PCE and FF variations with different active layer components (Ternary represents PM6:BTP-eC9:L8-BO; quaternary means PM6:BTP-eC9:L8-BO:BTP-S10).

parallel-like phase formation. The interfacial location of L8-BO in the host donor/acceptor (D/A) blend creates the extra charge transport channels, thus facilitating the exciton separation and carrier transport. It's noted that the $\omega_{\text{BTP-S10}}$ is −1.31 for the PM6:BTP-eC9:BTP-S10 blend, and −1.08 for the quaternary blend. The results confirm that BTP-S10 lies in the domain of

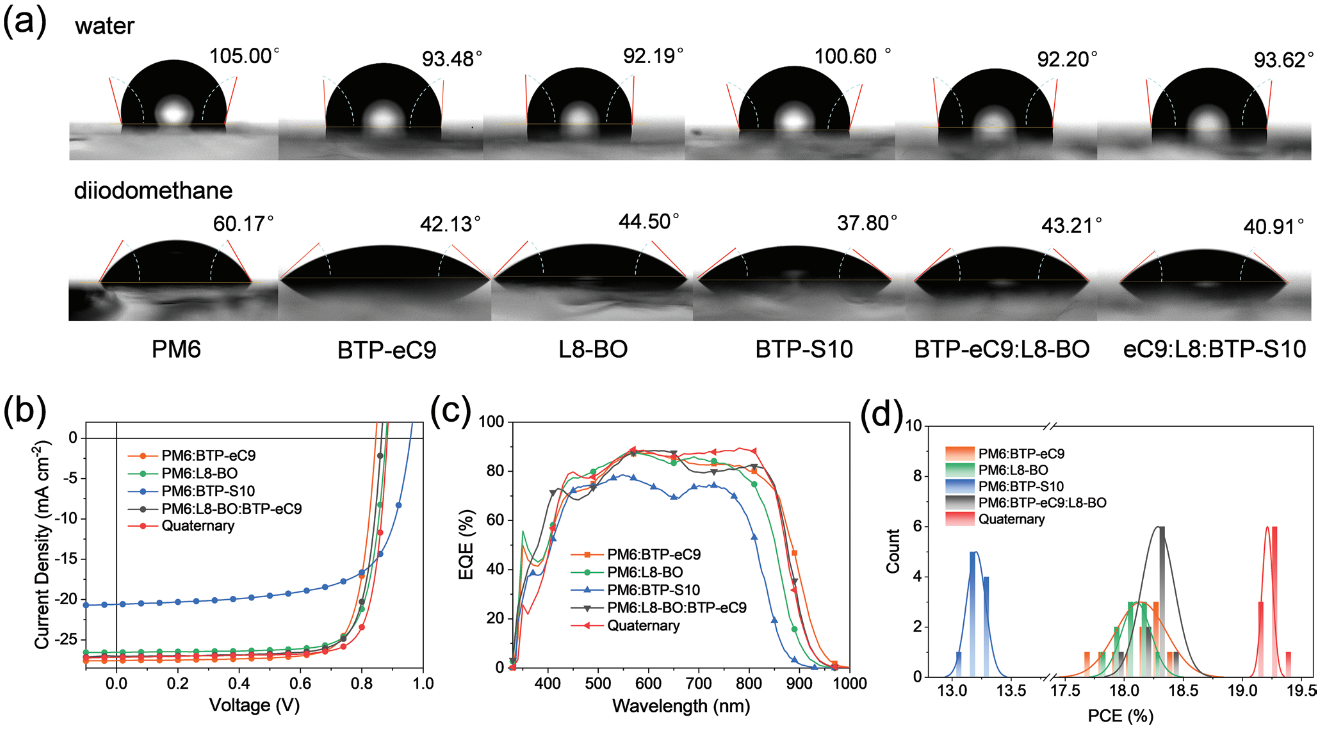

Figure 2. a) Contact angle images of various films with water and diiodomethane droplet on top. b) J–V curves, c) EQE curves, and d) histograms of PCE values for various binary, ternary and quaternary OPVs.

BTP-eC9 in both ternary (PM6:BTP-eC9:BTP-S10) and quaternary blends, resulting in the formation of BTP-eC9:BTP-S10 alloy-like phase, thus may boosting the domain purity of PM6 for the higher carrier mobility. In addition, BTP-S10 and L8-BO will form the parallel-like phase morphology when mixed with PM6 ($\omega_{\text{BTP-S10}}$ is −0.88 for PM6:L8-BO:BTP-S10 blend), which was also confirmed in our previous work.[46] So, the multiphase morphology could be realized in this quaternary blend.

To further confirm the formation of BTP-eC9:BTP-S10 alloy-like phase, differential scanning calorimetry (DSC) was applied to check the changes in melting and crystallization behaviors of mixed acceptors (BTP-eC9:BTP-S10, 5:2 by weight). The melting and crystallization points of BTP-eC9:BTP-S10 mixture changes obviously compared with those of the two pure acceptors, indicating the formation of an alloy-like phase (Figure S1, Supporting Information). The mixed acceptors also show elevated LUMO (−3.98 eV) and HOMO (−5.57 eV) levels compared with those of BTP-eC9 demonstrated by cyclic voltammetry (CV) (Figure S2, Supporting Information). This further proves the alloy-like phase formation. The elevated energy level of the acceptor could improve the V_{OC} value of the quaternary device.

2.2. Photovoltaic Properties

The conventional device structure was applied to construct the OPVs for investigating photovoltaic performances. Fabrication details can be found in Supporting Information. Figure 2b shows the J–V curves of the optimal binary, ternary (PM6:BTP-eC9:L8-BO), and quaternary devices, and relevant photovoltaic parameters are summarized in **Table 1**. The PM6:BTP-eC9 based binary device shows a high short-circuit current density (J_{SC}) of 27.59 mA cm^{-2}, and the PM6:BTP-S10 device displays the highest V_{OC} of 0.958 V. Both BTP-eC9 and L8-BO-based binary devices achieve a good PCE of over 18%, benefiting from the suitable photocurrent and fill factor (FF). The PM6:BTP-eC9:L8-BO ternary device shows reasonable changes in the V_{OC} and J_{SC} and produced a slightly improved PCE (Figure 1d). The increased FF of the ternary device may be related to the crystallinity and the phase separation of the ternary blend (this will be discussed in detail in the morphology parts). Notably, BTP-S10 exhibits the desired ability to reduce energy loss and could infuse into the domain of BTP-eC9, providing great possibility in enhancing the voltage and fining the oversized morphology by adding BTP-S10 as the fourth component. Finally, the optimal performance of the quaternary device is achieved with a D:A ratio of 1:0.6:0.6:0.2, delivering an outstanding PCE of 19.32% with an enhanced V_{OC} of 0.883 V, a higher J_{SC} of 27.17 mA cm^{-2}, and an enhanced FF of 80.49%. The optimal quaternary device was further certified by the National PV Industry Measurement and Testing Center (NPVIM), and a certified PCE of 19.35% (V_{OC} = 0.882 V, J_{SC} = 27.82 mA cm^{-2} and FF = 78.90%) was achieved (Figure S3, Supporting Information), which is the highest certified value for single-junction OPVs. The surprising results demonstrate that constructing an all-NFA quaternary blend via energy loss reduction and morphology optimization could achieve an efficiency breakthrough.

The EQE spectra of relevant devices are shown in Figure 2c. The PM6:BTP-eC9 shows a broad and high EQE, thus contributing to the high J_{SC}. The combination with L8-BO will lead to a blue-shifted absorption edge, resulting in a slightly decreased J_{SC}, but a higher V_{OC}. Furthermore, the addition of BTP-S10 causes the blue-shift of EQE edge but the V_{OC} could be significantly enhanced due to the mitigated E_{loss} (detailed analysis in Section 2.4). The higher EQE values in 450–550 nm may originate from the purer donor domain. The more delicate morphology of acceptors may cause a higher response between 650–850 nm, thus resulting in increased J_{SC}. The calculated $J_{\text{cal.}}$ from EQE is consistent with the measured J_{SC} from J–V curves with errors of ≈2% (Table 1). Figure 2d is the histograms of PCEs of various devices in this work, verifying the effectiveness and repeatability of our quaternary strategy.

Table 1. The photovoltaic parameters of the champion devices based on different acceptor components and solvents. Average parameters with standard deviation in parentheses were obtained from 10 individual devices.

D:A$_1$:A$_2$:A$_3$$^{a)}$	V_{OC} [V]	J_{SC} [mA cm^{-2}]	$J_{\text{cal}}$$^{b)}$ [mA cm^{-2}]	FF [%]	PCE [%]
1:1.2:0:0	0.845 (0.842 ± 0.002)	27.59 (27.65 ± 0.13)	26.95	78.49 (77.85 ± 0.65)	18.32 (18.14 ± 0.20)
1:0:1.2:0	0.878 (0.876 ± 0.002)	26.54 (26.45 ± 0.09)	25.68	78.29 (78.09 ± 0.27)	18.27 (18.27 ± 0.12)
1:0:0:1.2	0.958 (0.954 ± 0.002)	20.60 (20.72 ± 0.01)	20.67	67.50 (66.82 ± 0.40)	13.32 (13.20 ± 0.08)
1:0.6:0.6:0	0.864 (0.861 ± 0.004)	27.04 (27.13 ± 0.25)	25.99	78.81 (78.44 ± 0.40)	18.37 (18.29 ± 0.13)
1:0.5:0.5:0.2	0.883 (0.884 ± 0.002)	27.17 (27.28 ± 0.08)	26.62	80.49 (79.66 ± 0.46)	19.32 (19.21 ± 0.04)
1:0.5:0.5:0.2$^{c)}$	0.882	27.82	/	78.90	19.35
1:0.5:0.5:0.2$^{d)}$	0.874 (0.872 ± 0.003)	27.12 (27.07 ± 0.09)	27.08	80.26 (79.94 ± 0.56)	19.07 (18.90 ± 0.12)

$^{a)}$A$_1$: BTP-eC9, A$_2$: L8-BO, A$_3$: BTP-S10; $^{b)}$Integrated current densities from EQE curves; $^{c)}$Certified result from the National PV Industry Measurement and Testing Center (NPVIM); $^{d)}$Quaternary device processed with toluene.

2.3. Behaviors of Excitons and Charges

Since the carrier behaviors are closely related to the morphology, we analyzed the charge dynamics (charge generation, transportation, and recombination) to explore the role of multiphase morphology on photovoltaic performance. Photoluminescence spectroscopy (PL) and time-resolved photoluminescence spectroscopy (TRPL) were applied to investigate the energy transfer, charge transfer between acceptors and exciton separation in different films (**Figure 3**a and Figure S4, Supporting Information). The emission intensity of L8-BO could be enhanced by mixing with BTP-S10 (Figure S4a, Supporting Information), indicating energy transfer from BTP-S10 to L8-BO. The reduced exciton lifetime in L8-BO:BTP-S10 blend films also indicates charge transfer from BTP-S10 to L8-BO. When BTP-eC9 and L8-BO are mixed, the emission intensity of BTP-eC9 is weakened, indicating that energy transfer could not occur between BTP-eC9 and L8-BO, but charge transfer might occur from L8BO to BTP-eC9 which is verified by reduced TRPL lifetime. When BTP-S10 is mixed with BTP-eC9:L8-BO blend, the reduced TRPL lifetime also indicates charge transfer from BTP-S10 to BTP-eC9. On the other hand, NFA films show long exciton lifetimes (898.47 ps for BTP-eC9, 730.06 ps for BTP-eC9:L8-BO, and 705.30 ps for BTP-eC9:L8-BO:BTP-S10). The blend films show a fast PL decay due to the fast interfacial charge transfer (or exciton separation). The ternary blend shows a shorter lifetime (80.53 ps) than that (88.66 ps) of the PM6:BTP-eC9 blend due to the parallel-like phase in the ternary blend, indicating better exciton dissociation. With the addition of BTP-S10, the morphology was optimized, thus further boosting the exciton dissociation which is demonstrated by the faster decay lifetime (74.40 ps). The improved charge generation and charge transfer between acceptors are believed to allow better construction of the thick-film and large-area devices.

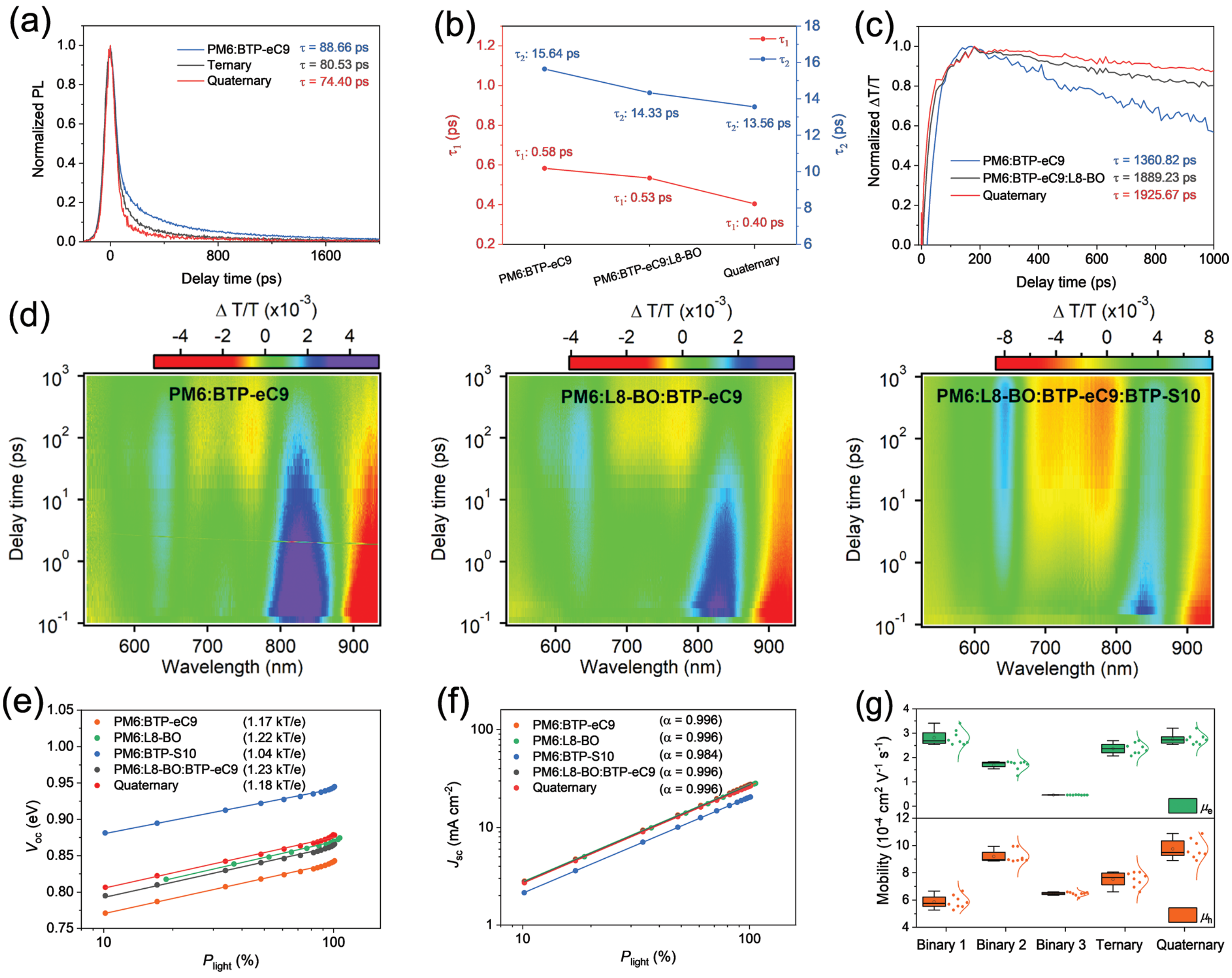

Figure 3. a) TRPL of PM6:BTP-eC9, ternary and quaternary films probed at 850–950 nm. b) Comparison of τ_1 and τ_2 of different blends. c) Time evolution of GSB signal of PM6:BTP-eC9, ternary and quaternary films at indicated fluences with 800 nm excitation. d) Color plot of TA spectra of PM6:BTP-eC9, ternary and quaternary films under 800 nm excitation. e,f) Dependence of V_{OC} (e) and J_{SC} (f) on light intensity of the binary, ternary and quaternary OPVs. g) Electron and hole mobilities of different devices (Binary 1 is PM6:BTP-eC9, Binary 2 is PM6:L8-BO, Binary 3 is PM6:BTP-S10, Ternary is PM6:BTP-eC9:L8-BO, and Quaternary is PM6:BTP-eC9:L8-BO:BTP-S10, the error bars are defined as the standard deviation, which is calculated from eight devices).

Then, the charge-transfer kinetics and carrier lifetime of these OPV systems were studied via transient absorption spectroscopy (TAS). Figure 3b (Figure S5, Supporting Information) is the hole-transfer kinetics, and Figure 3c is the charge-carrier lifetime that extracted from the TA data. Figure 3d show the TA data recorded from the various blends (PM6:BTP-eC9, ternary, quaternary) were excited at 800 nm. It's found that both of the time constants τ_1 (0.58, 0.53, and 0.40 ps for PM6:BTP-eC9, ternary and quaternary blends, respectively) and τ_2 (15.64, 14.33, and 13.56 ps for the PM6:BTP-eC9, ternary and quaternary blends, respectively) are gradually reduced in ternary and quaternary blend compared to the binary blend (Figure 3b). The τ_1 represents the dissociation times of excitons at the D/A interfaces. The τ_2 illustrates the time that excitons diffuse to the interfaces.[47] The exciton separation and transportation were enhanced in the quaternary system, which may benefit from the exquisite morphology, and consisted well with the TRPL results.

Comparing the TA signals of neat NFA films (Figure S7, Supporting Information) and blend films (Figure 3d and Figure S6, Supporting Information), a new bleach signal near 650 nm appears for blend films, induced by hole transfer from the NFAs to PM6. The additional excited-state absorption (ESA) features at 700–800 nm suggest that excitations occupied the acceptor and electron sites associated with the charge-separated (CS) state of free polarons reported in the literature.[48] Further, the carrier lifetimes are extracted by intercepting the dynamics at this position and fitting the falling edge of the dynamics. As shown in Figure 3c, the carrier lifetime of the quaternary blend ($\tau = 1925.67$ ps) is much longer than that of binary ($\tau = 1360.82$ ps for PM6:BTP-eC9) and ternary ($\tau = 1889.23$ ps for PM6:BTP-eC9:L8-BO). Enlarged carrier lifetime plays a crucial role in realizing the high efficiency of thick-film and large-area OPVs.

The charge recombination dynamics of OPVs were studied by measuring *J*–*V* curves under various light intensities (P_{light}). The relationship between V_{oc} and P_{light} can be used to describe the monomolecular recombination (nkT/q, q is the elementary charge, k is the Boltzmann constant, and T is the absolute temperature). As shown in Figure 3e, the slopes of the ternary device are highest at $1.23kT/q$ due to the oversized separated phase in the blend, resulting in severe monomolecular recombination. The slope is decreased obviously ($1.17kT/q$), benefiting from the more proper morphology of the quaternary blend, which indicates that monomolecular recombination is reduced in the quaternary device. The bimolecular recombination could be represented via the relation of $J_{\text{sc}} \propto P_{\text{light}}{}^{\alpha}$ (the α value is the exponential factor, which closer to 1 means less bimolecular recombination). The bimolecular recombination showed a similar situation for all devices, except for the BTP-S10-based binary device that suffers from the large domains as depicted in AFM images. The reduced monomolecular and bimolecular recombination contributes to the higher FF of the quaternary device.

To measure the charge-transport properties of OPVs, the space charge limited current (SCLC) method was applied, as shown in Figure 3g and Figure S8, and Table S3, Supporting Information. Hole mobility (μ_h) of the ternary device is 7.52×10^{-4} cm^2 V^{-1} s^{-1}, which is in the middle compared to their host binary systems (5.78×10^{-4} cm^2 V^{-1} s^{-1} for PM7:BTP-eC9, 9.20×10^{-4} cm^2 V^{-1} s^{-1} for PM6:L8-BO). The electron mobilities (μ_e) of the ternary device show a similar trend. While for the quaternary system, the formation of an alloy-like phase enhances the donor purity, thus boosting the hole mobility (9.75×10^{-4} cm^2 V^{-1} s^{-1}), and the high electron mobility (2.76×10^{-4} cm^2 V^{-1} s^{-1}) is maintained due to the optimized morphology. Therefore, the quaternary OPV shows the highest hole and electron mobility, thus beneficial for high J_{SC} and FF and thick-film and large-area OPVs.

2.4. Energy Loss

Except for the enhanced J_{SC} and FF, the higher V_{OC} is also the main factor in achieving the high efficiency of the quaternary device. It's necessary to conduct a detailed analysis of the E_{loss} for the various OPVs. The E_{loss} consists of three parts.[49] ΔE_1 is the radiative recombination, an unavoidable part derived from the absorption above the bandgap. ΔE_2 is the radiative recombination (below the bandgap) loss, which is affected by the degree of energy disorder and reorganization. ΔE_3 is the nonradiative recombination, which could be calculated via the luminescence efficiency of photovoltaic devices.

The EL and the Fourier transform photocurrent spectroscopy (FTPS)-EQE (**Figure 4**a–e) were carried out to examine the E_{loss}. The detailed data of E_{loss} for the various OPVs are listed in **Table 2**, and the calculation methods are described in the Supporting Information. Notably, the significantly higher ΔE_2 of the ternary device delivered the severe E_{loss}. As shown in Figure 4d, a more significant Urbach energy parameter (E_{U}) is figured out in the ternary device, indicating its higher energy disorder degree.[50] The Stokes shift between UV–vis absorption and PL spectra indicates the level of reorganization energy, which is another indicator of energy disorder.[10] A larger Stokes shift could be found in the ternary blend (Figure S9, Supporting Information), thus resulting in notable E_{loss}. With the addition of BTP-S10, the values of ΔE_2 are reduced, resulting from the lowered degree of energy disorder (lower E_{U} of 25.99 eV and smaller Stokes shift of 117.3 nm). Calculating from the electroluminescence quantum efficiency (EQE_{EL}), the value of ΔE_3 was also mitigated,[51] which benefited from the high luminescence efficiency of the BTP-S10-based devices (Figure 4e), thus quaternary device exhibiting the lower E_{loss} and a higher V_{OC}.

2.5. Film Morphology

Atomic force microscopy (AFM) was used to explore the top surface structure and aggregation properties. As shown in **Figure 5**a, the PM6:BTP-eC9 and the PM6:L8-BO film show a smooth surface with small roughness (root-mean-square, RMS) of 1.05 and 0.97 nm, due to the good miscibility between BTP-eC9/L8-BO and PM6. In contrast, the PM6:BTP-S10 film exhibited a more rough (RMS = 2.23 nm) surface than other binary films, confirming the worse compatibility between BTP-S10 and PM6. For the ternary and quaternary blend, the roughness is similar to each other, resulting in the same bimolecular recombination. The corresponding AFM phase images are shown in Figure S10 (Supporting Information).

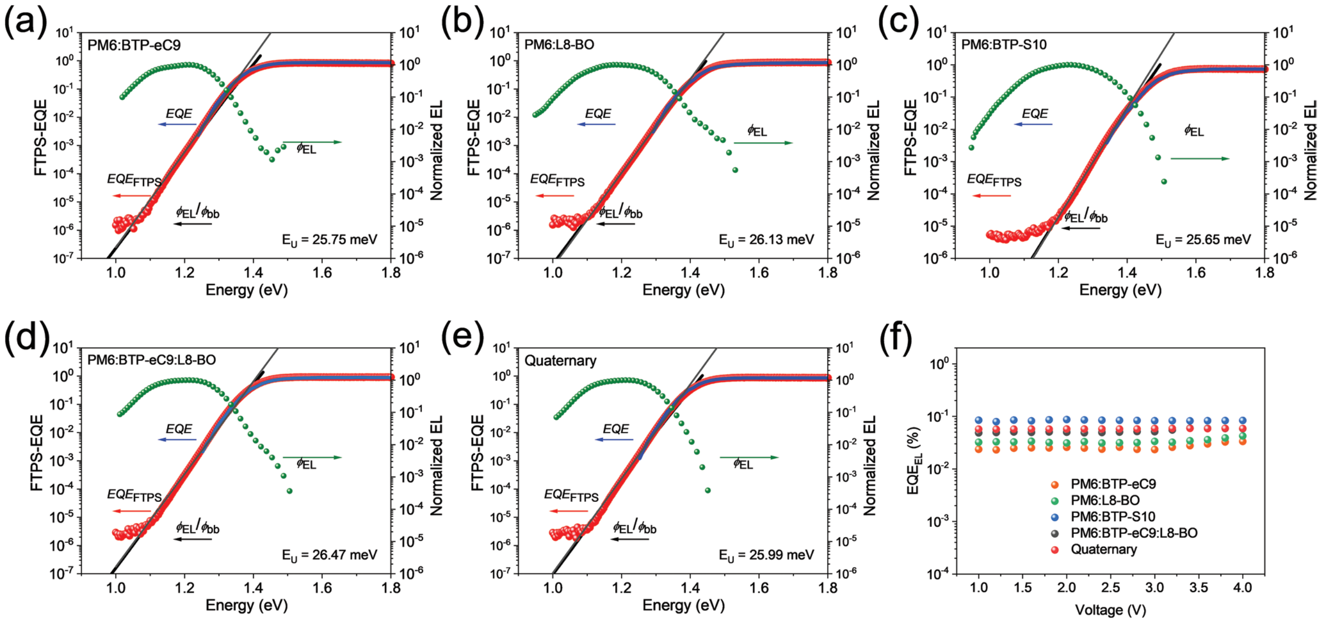

Figure 4. a–e) Semilogarithmic plots of normalized EL spectra, measured EQE spectra, and FTPS-EQE spectra as a function of energy for devices based on PM6:BTP-eC9 (a); PM6:L8-BO (b); PM6:BTP-S10 (c); PM6:BTP-eC9:L8-BO (d); and quaternary blends (e). f) EQE_{EL} of OPVs with different components at various bias voltages.

The nanomorphology, such as intermixing and domain phases within the active layer, were further studied using the grazing-incidence transmission small-angle X-ray scattering (GTSAXS) technique.[52] Figure 5b displays the 2D-scattering patterns of various blend films, and the corresponding in-plane (IP) and out-of-plane (OOP)-scattering profiles are shown in Figure 5c and Figure 5d, and the phase sizes are listed in Table S4 (Supporting Information). PM6:L8-BO blend possesses stronger crystallinity (as demonstrated in the GIWAXs), which may contribute to the larger intermixing phase size of 55 nm, and larger domain size (29 nm for both in IP and OOP direction, Table S4, Supporting Information). Moreover, the ternary blend presents an intermixing phase size of 50 nm. This oversized nanomorphology leads to severe monomolecular recombination as demonstrated previously. Notably, both the intermixing phase size (35 nm) and the domain size (25 nm for IP direction and 24 nm for OOP direction) of the quaternary blend are reduced, indicating the formation of an exquisite nanomorphology, thus promoting the preferable carrier behavior in the quaternary device.

The orientation and packing of molecules were investigated by grazing-incidence wide-angle X-ray scattering (GIWAXS) measurement, as shown in Figures S11 and S12 (Supporting Information). The crystalline coherence length (CCL, Table S5, Supporting Information) and the azimuthal integration (Table S6, Supporting Information) are calculated to investigate the relative degree of crystallinity of these systems.[53,54] The CCL of (100) lamellar diffraction peak (CCL = 84.4 nm) and the (010) π–π stacking peak (CCL = 21.4 nm) of the ternary blend film are shorter than those of the PM6: BTP-eC9 binary blend (CCL is 78.0 and 21.1 nm), indicating that the crystallinity is weakened to a certain extent. The quaternary film shows an enhanced CCL value (78.8 and 21.1 nm) by adding BTP-S10, indicating increased crystallinity. What's more, we found that both the (100) lamellar stacking of face-on orientation ($A_{\text{face-on}}/A_{\text{edge-on}}$ is 1.40) and π–π stacking direction ($A_{\text{face-on}}/A_{\text{edge-on}}$ is 4.25) are significantly enhanced in the quaternary blend compared with those of binary and ternary blend, which is beneficial to the charge transport in the vertical direction. This indicates the introduction of BTP-S10 is beneficial for the nanomorphology optimization without destroying the crystallinity. These improvements contribute to the enhanced charge transport properties of the quaternary blend films, as demonstrated by SCLC.

Table 2. Detailed energy losses of OPVs based on different acceptor components.

Active layer	E_g [eV]	qV_{OC} [eV]	E_{loss} [eV]	qV_{OC}^{SQ} [eV]	qV_{OC}^{rad} [eV]	ΔE_1 [eV]	ΔE_2 [eV]	ΔE_3 [eV]	Exp. $q\Delta V_{OC}^{nonrad}$ [eV]	EQE_{EL} [%]
PM6:BTP-eC9	1.378	0.850	0.528	1.125	1.060	0.252	0.065	0.210	0.213	2.61×10^{-2}
PM6:L8-BO	1.441	0.878	0.562	1.183	1.087	0.257	0.096	0.208	0.207	3.36×10^{-2}
PM6:BTP-S10	1.475	0.954	0.521	1.188	1.131	0.257	0.057	0.178	0.183	8.34×10^{-2}
PM6:BTP-eC9:L8-BO	1.425	0.867	0.558	1.170	1.061	0.255	0.109	0.194	0.195	5.23×10^{-2}
Quaternary	1.425	0.882	0.543	1.170	1.073	0.255	0.097	0.191	0.193	5.77×10^{-2}

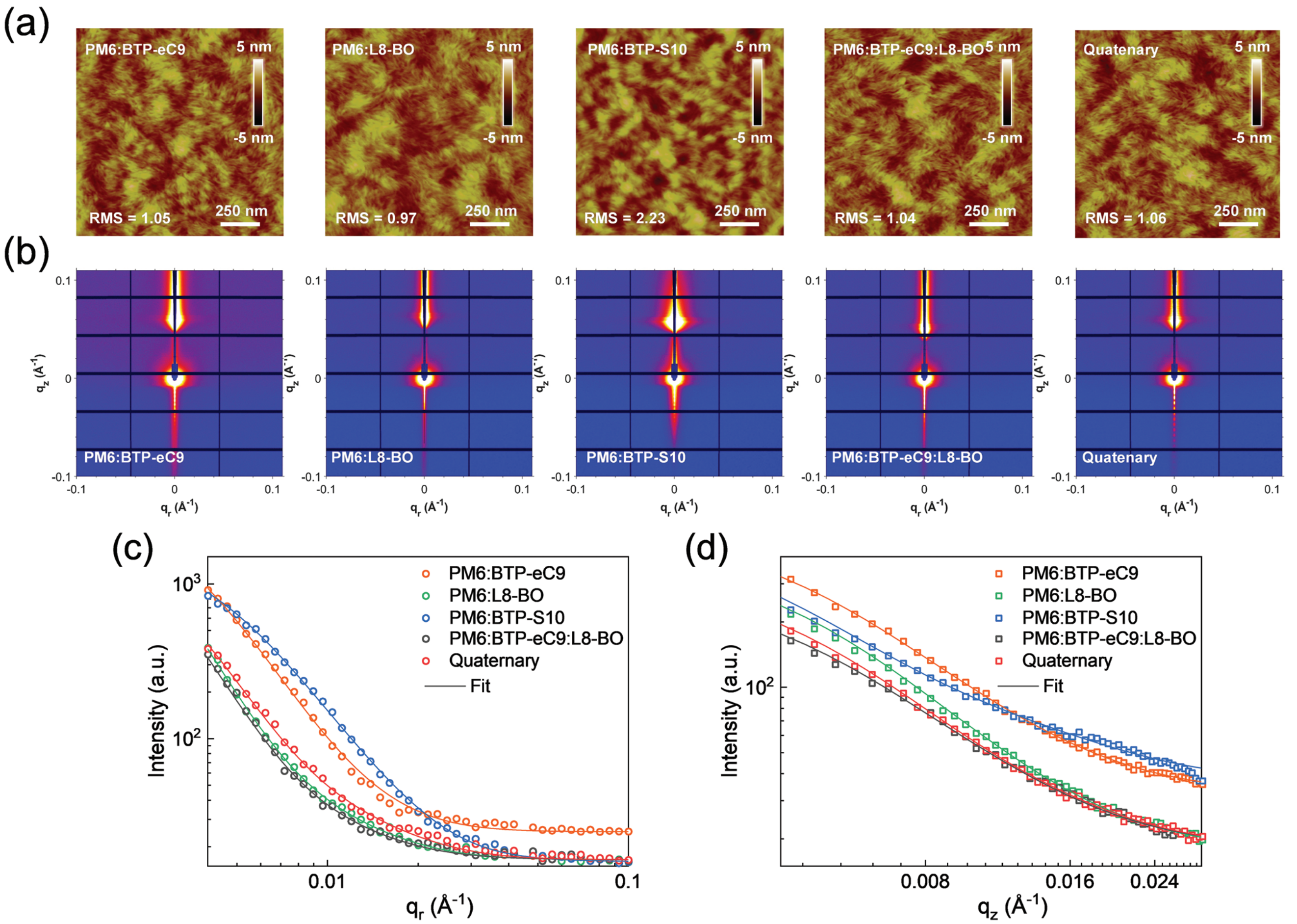

Figure 5. a) AFM height images of PM6:BTP-eC9, PM6:L8-BO, PM6:BTP-S10, PM6:BTP-eC9 and quaternary films. b) 2D GTSAXS images of relevant binary, ternary and quaternary blends. c,d) GTSAXS in-plane (c) and out-of-plane (dscattering profiles for various blend films.

2.6. Toluene-Processed Devices

Chloroform is a volatile solvent with a low boiling point of 61 °C, thus it is difficult to control the film drying during blading coating or other printing technologies for large-area modules. It is also highly toxic and is not suitable for OPV commercialization. The performance of the device processed with environmentally friendly solvents should be investigated. Here, the quaternary device processed with toluene was fabricated, and the corresponding parameters are listed in Table 1 (Figure S13a,b, Supporting Information). The toluene-processed small device shows a high efficiency of 19.07%, with a V_{OC} of 0.87 V, a J_{SC} of 27.12 mA cm^{-2}, and a FF of 80.26%. The high performance is due to the low recombination (the slope of the device is 1.02kT/q, and α is 0.998, as shown in Figure S13c, Supporting Information), high electron mobility (Figure S13d, Supporting Information), and fine morphology (Figure S14, Supporting Information).

2.7. Large-Area Devices and Modules

A scheme that illustrates the carrier behaviors of the quaternary blend is shown in **Figure 6**a, in which the multiphase morphology (parallel-like and alloy-like phase) and the superior carrier behaviors (efficient exciton separation, high carrier mobility, and long carrier lifetime) can be found and are proved in previous sections. To verify the advantages of this quaternary system for upscaling, we fabricated quaternary devices with different areas (1.05 and 72.25 cm^2). The quaternary large-area (1.05 cm^2) devices deliver a surprising PCE of 18.25% (Figure 6b), with a J_{SC} of 27.43 mA cm^{-2} and a desirable FF of 74.81%, indicating the uniform morphology obtained during the drying process. Further, the quaternary system was used to fabricate large-area modules via blade-coating in air utilizing an environmentally friendly solvent (toluene) without any additives with a total module area of 72.25 cm^2 (active area is 67.915 cm^2) (Figure 6c), which is crucial for commercial fabrication. The large-area modules are interconnected by 17 sub-cells with an area of 0.5 × 8.5 cm^2 for each sub-cell. The geometric fill factor (GFF) is 0.94. The large-area module shows a high PCE of 12.20% with respect to the total module area, with a V_{OC} of 14.28 V, a J_{SC} of 1.22 mA cm^{-2}, and an FF of 70.20%. Figure 6d shows the development status of large-area devices. Our works are also among the highest ones (Table S8, Supporting Information).

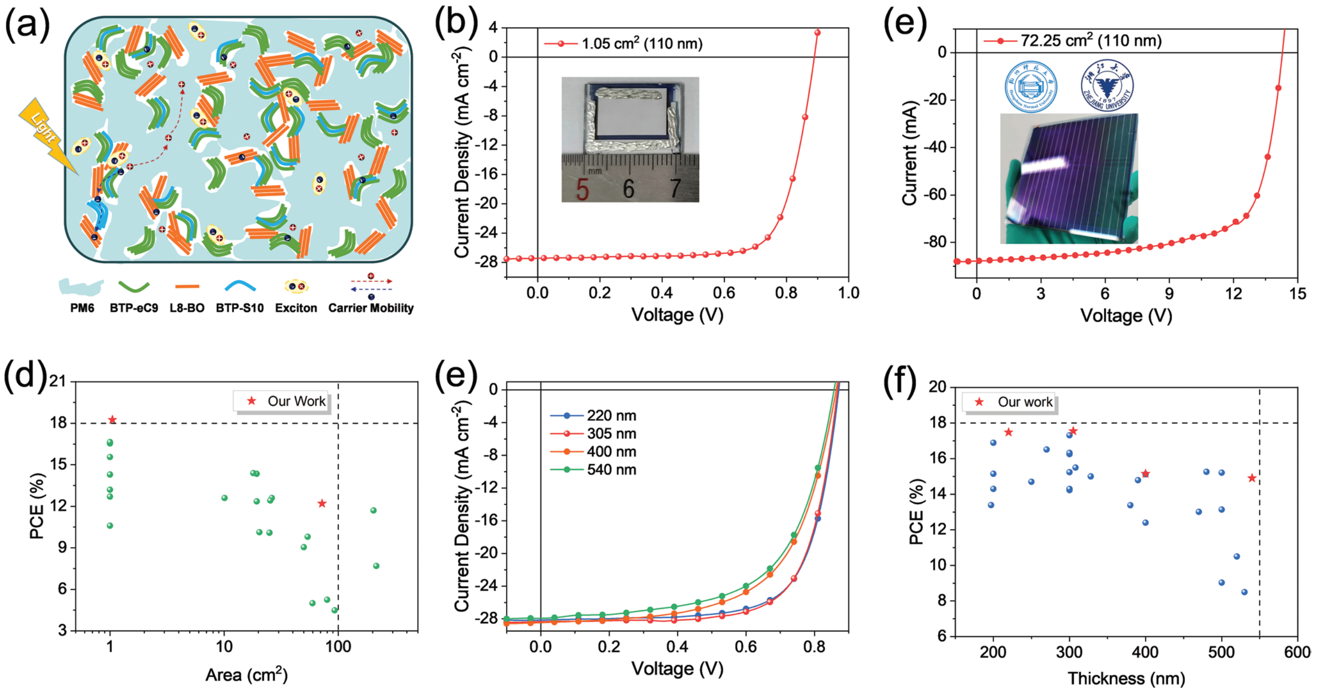

Figure 6. a) Schematic of carrier dynamics in quaternary OPV. b,c) The *J*–*V* curves of the large-area devices with device areas of 1.05 cm^2 (b) and 72.25 cm^2 (c) (the insets are the photos of the corresponding devices). d) Development status of large-area devices. e) *J*–*V* curves of thick-film devices. f) The development status of thick-film devices with different thicknesses.

2.8. Thick-Film Devices

Moreover, the quaternary devices with different thicknesses (≈200, ≈300, ≈400, and ≈500 nm) were fabricated to verify the advantages of this quaternary system for higher thickness tolerance. Figure 6e shows the *J*–*V* curves of quaternary devices with various thicknesses, and the corresponding parameters of these devices are summarized in **Table 3**. Impressively, with the thickness increase, the J_{SC} of OPVs improved gradually and could keep over 28 mA cm^{-2} with a thickness of ≈500 nm. The ≈300 nm thickness device presents an outstanding PCE of 17.55%. The reduced PCE is mainly due to the dramatically decreased FF, which is attributed to severe bimolecular recombination in thicker-film devices demonstrated by the decreased α value from 0.996 to 0.992 and to 0.980 for the devices based on 110, 305, and 540 nm films respectively (Figure S15, Supporting Information). The binary device based on PM6:BTP-eC9 with 305 nm-thick film shows a PCE of 16.35% (Table S7, Supporting Information) with more serious bimolecular recombination (α = 0.987). The results further confirm the advantage of the quaternary strategy with higher film thickness tolerance. Figure 6f shows the development status of thick-film

Table 3. The photovoltaic parameters of the champion devices based on quaternary system with different thicknesses and device areas. Average parameters with standard deviation in parentheses were obtained from 10 individual devices.

Device condition		V_{OC} [V]	J_{SC} [mA cm^{-2}]	FF [%]	PCE [%]
Thickness [nm]	Area [cm^{-2}]				
110	0.0473	0.883 (0.884 ± 0.002)	27.17 (27.28 ± 0.08)	80.49 (79.66 ± 0.46)	19.32 (19.21 ± 0.04)
220	0.0473	0.871 (0.871 ± 0.001)	28.16 (27.46 ± 0.50)	71.19 (71.53 ± 0.72)	17.48 (17.12 ± 0.21)
305	0.0473	0.867 (0.867 ± 0.001)	28.35 (27.93 ± 0.59)	71.30 (70.69 ± 0.88)	17.55 (17.14 ± 0.33)
400	0.0473	0.863 (0.865 ± 0.001)	28.47 (28.53 ± 0.20)	61.70 (60.45 ± 1.10)	15.14 (14.89 ± 0.16)
540	0.0473	0.863 (0.860 ± 0.002)	28.24 (28.14 ± 0.27)	61.29 (59.96 ± 1.44)	14.90 (14.49 ± 0.31)
110	1.05	0.889 (0.885 ± 0.005)	27.43 (27.03 ± 0.35)	74.81 (74.95 ± 0.35)	18.25 (18.00 ± 0.15)
110	72.25	14.28	1.22	70.20	12.20

devices of various thicknesses, and our PCEs are among the highest ones (Table S9, Supporting Information).

3. Conclusions

A quaternary strategy was used to efficiently construct the multiphase morphology and mitigate the energy loss to achieve an outstanding PCE of 19.32% (certified 19.35%). The desirable carrier behaviors with efficient exciton dissociation, high carrier mobility, long carrier lifetime, and reduced charge recombination are confirmed with detailed analyses of the carrier dynamics. The exquisite multiphase morphology is verified by the wetting coefficient and GTSAXs measurement. Encouraged by the superior carrier behaviors and smaller domain size favorable for the thickness tolerance and upscaling, large-area devices (110 nm) and thick-film devices (0.0473 cm^2) were fabricated. The large-area devices (1.05 and 72.25 cm^2) with 110 nm thickness show excellent PCEs of 18.25% and 12.20%, and the quaternary device with ≈300 nm-thick active layer exhibits a high PCE of 17.55%. These achievements provide fundamental insight into the importance of carrier behaviors and intermixing phase size for fabricating large-area and thick-film devices, promoting the quaternary strategy of OPV for commercialization.

Supporting Information

Supporting Information is available from the Wiley Online Library or from the author.

Acknowledgements

L.Z. and Y.L. contributed equally to this work. This work was supported by the National Natural Science Foundation of China (Nos. 5212780017, 21734008, 51803178, 61721005, 52103324), National Key Research and Development Program of China (No. 2019YFA0705900) and the China Postdoctoral Science Foundation funded project (No. 2022M712737). L. Z. acknowledge the research start-up fund from Hangzhou Normal University (4095C50222204002). The authors also thank the beam time and technical supports provided by 19U2 beamline at SSRF, Shanghai. The financial support from the National Key Research and Development Program of China (Nos. 2017YFA0207700, 2019YFA0705902) was also appreciated.

Conflict of Interest

The authors declare no conflict of interest.

Data Availability Statement

Research data are not shared.

Keywords

carrier lifetime, large-area devices, multiphase morphology, quaternary organic photovoltaics, thick films

Received: July 11, 2022
Revised: September 3, 2022
Published online: October 10, 2022

[1] Y. Li, C. He, L. Zuo, F. Zhao, L. Zhan, X. Li, R. Xia, H.-L. Yip, C.-Z. Li, X. Liu, H. Chen, *Adv. Energy Mater.* **2021**, *11*, 2003408.
[2] D. Wang, R. Qin, G. Zhou, X. Li, R. Xia, Y. Li, L. Zhan, H. Zhu, X. Lu, H.-L. Yip, H. Chen, C.-Z. Li, *Adv. Mater.* **2020**, *32*, 2001621.
[3] W. Liu, S. Sun, S. Xu, H. Zhang, Y. Zheng, Z. Wei, X. Zhu, *Adv. Mater.* **2022**, *34*, 2200337.
[4] Z. Zheng, J. Wang, P. Bi, J. Ren, Y. Wang, Y. Yang, X. Liu, S. Zhang, J. Hou, *Joule* **2022**, *6*, 171.
[5] X. Zheng, L. Zuo, F. Zhao, Y. Li, T. Chen, S. Shan, K. Yan, Y. Pan, B. Xu, C.-Z. Li, M. Shi, J. Hou, H. Chen, *Adv. Mater.* **2022**, *34*, 2200044.
[6] J. Yuan, Y. Zhang, L. Zhou, G. Zhang, H.-L. Yip, T.-K. Lau, X. Lu, C. Zhu, H. Peng, P. A. Johnson, M. Leclerc, Y. Cao, J. Ulanski, Y. Li, Y. Zou, *Joule* **2019**, *3*, 1140.
[7] S. Li, L. Zhan, F. Liu, J. Ren, M. Shi, C.-Z. Li, T. P. Russell, H. Chen, *Adv. Mater.* **2018**, *30*, 1705208.
[8] M. Zhang, X. Guo, W. Ma, H. Ade, J. Hou, *Adv. Mater.* **2015**, *27*, 4655.
[9] Y. Lin, J. Wang, Z.-G. Zhang, H. Bai, Y. Li, D. Zhu, X. Zhan, *Adv. Mater.* **2015**, *27*, 1170.
[10] L. Zhan, S. Li, Y. Li, R. Sun, J. Min, Z. Bi, W. Ma, Z. Chen, G. Zhou, H. Zhu, M. Shi, L. Zuo, H. Chen, *Joule* **2022**, *6*, 662.
[11] S. Li, L. Zhan, Y. Jin, G. Zhou, T.-K. Lau, R. Qin, M. Shi, C.-Z. Li, H. Zhu, X. Lu, F. Zhang, H. Chen, *Adv. Mater.* **2020**, *32*, 2001160.
[12] K. Chong, X. Xu, H. Meng, J. Xue, L. Yu, W. Ma, Q. Peng, *Adv. Mater.* **2022**, *34*, 2109516.
[13] Y. Cui, Y. Xu, H. Yao, P. Bi, L. Hong, J. Zhang, Y. Zu, T. Zhang, J. Qin, J. Ren, Z. Chen, C. He, X. Hao, Z. Wei, J. Hou, *Adv. Mater.* **2021**, *33*, 2102420.
[14] L. Zhu, M. Zhang, J. Xu, C. Li, J. Yan, G. Zhou, W. Zhong, T. Hao, J. Song, X. Xue, Z. Zhou, R. Zeng, H. Zhu, C.-C. Chen, R. C. I. MacKenzie, Y. Zou, J. Nelson, Y. Zhang, Y. Sun, F. Liu, *Nat. Mater.* **2022**, *21*, 656.
[15] C. He, Y. Pan, Y. Ouyang, Q. Shen, Y. Gao, K. Yan, J. Fang, Y. Chen, C.-Q. Ma, J. Min, C. Zhang, L. Zuo, H. Chen, *Energy Environ. Sci.* **2022**, *15*, 2537.
[16] L. Zuo, S. B. Jo, Y. Li, Y. Meng, R. J. Stoddard, Y. Liu, F. Lin, X. Shi, F. Liu, H. W. Hillhouse, D. S. Ginger, H. Chen, A. K. Y. Jen, *Nat. Nanotechnol.* **2022**, *17*, 53.
[17] Y. Li, Y. Guo, Z. Chen, L. Zhan, C. He, Z. Bi, N. Yao, S. Li, G. Zhou, Y. Yi, Y. Yang, H. Zhu, W. Ma, F. Gao, F. Zhang, L. Zuo, H. Chen, *Energy Environ. Sci.* **2022**, *15*, 855.
[18] S. Li, L. Zhan, N. Yao, X. Xia, Z. Chen, W. Yang, C. He, L. Zuo, M. Shi, H. Zhu, X. Lu, F. Zhang, H. Chen, *Nat. Commun.* **2021**, *12*, 4627.
[19] M. Moser, A. Wadsworth, N. Gasparini, I. McCulloch, *Adv. Energy Mater.* **2021**, *11*, 2100056.
[20] F. Eisner, J. Nelson, *Joule* **2021**, *5*, 1319.
[21] G. Bernardo, T. Lopes, D. G. Lidzey, A. Mendes, *Adv. Energy Mater.* **2021**, *11*, 2100342.
[22] D. Zhang, B. Fan, L. Ying, N. Li, C. J. Brabec, F. Huang, Y. Cao, *SusMat* **2021**, *1*, 4.
[23] N. Tokmoldin, S. M. Hosseini, M. Raoufi, L. Q. Phuong, O. J. Sandberg, H. Guan, Y. Zou, D. Neher, S. Shoaee, *J. Mater. Chem. A* **2020**, *8*, 7854.
[24] Y. Cai, Q. Li, G. Lu, H. S. Ryu, Y. Li, H. Jin, Z. Chen, Z. Tang, G. Lu, X. Hao, H. Y. Woo, C. Zhang, Y. Sun, *Nat. Commun.* **2022**, *13*, 2369.
[25] A. Classen, C. L. Chochos, L. Lüer, V. G. Gregoriou, J. Wortmann, A. Osvet, K. Forberich, I. McCulloch, T. Heumüller, C. J. Brabec, *Nat. Energy* **2020**, *5*, 711.
[26] C. Cui, Y. Li, *Aggregate* **2021**, *2*, e31.
[27] T. Wang, G. Kupgan, J.-L. Brédas, *Trends Chem.* **2020**, *2*, 535.
[28] X. Xu, Y. Li, Q. Peng, *Adv. Mater.* **2022**, https://doi.org/10.1002/adma.202107476.

[29] J. Xu, S. B. Jo, X. Chen, G. Zhou, M. Zhang, X. Shi, F. Lin, L. Zhu, T. Hao, K. Gao, Y. Zou, X. Su, W. Feng, A. K.-Y. Jen, Y. Zhang, F. Liu, *Adv. Mater.* **2022**, *34*, 2108317.

[30] Y. Ni, X. Liu, Y. Liu, Z. Feng, D. Tu, X. Guo, C. Li, *ACS Appl. Mater. Interfaces* **2022**, *14*, 12461.

[31] L. Zhan, S. Li, T.-K. Lau, Y. Cui, X. Lu, M. Shi, C.-Z. Li, H. Li, J. Hou, H. Chen, *Energy Environ. Sci.* **2020**, *13*, 635.

[32] N. Y. Doumon, L. Yang, F. Rosei, *Nano Energy* **2022**, *94*, 106915.

[33] K.-N. Zhang, X.-Y. Du, Z.-H. Chen, T. Wang, Z.-Q. Yang, H. Yin, Y. Yang, W. Qin, X.-T. Hao, *Adv. Energy Mater.* **2022**, *12*, 2103371.

[34] Z. Jia, Z. Chen, X. Chen, J. Yao, B. Yan, R. Sheng, H. Zhu, Y. Yang, *Photon. Res.* **2021**, *9*, 324.

[35] L. Arunagiri, Z. Peng, X. Zou, H. Yu, G. Zhang, Z. Wang, J. Y. Lin Lai, J. Zhang, Y. Zheng, C. Cui, F. Huang, Y. Zou, K. S. Wong, P. C. Y. Chow, H. Ade, H. Yan, *Joule* **2020**, *4*, 1790.

[36] M. Zhang, L. Zhu, G. Zhou, T. Hao, C. Qiu, Z. Zhao, Q. Hu, B. W. Larson, H. Zhu, Z. Ma, Z. Tang, W. Feng, Y. Zhang, T. P. Russell, F. Liu, *Nat. Commun.* **2021**, *12*, 309.

[37] Z. Peng, K. Jiang, Y. Qin, M. Li, N. Balar, B. T. O'Connor, H. Ade, L. Ye, Y. Geng, *Adv. Energy Mater.* **2021**, *11*, 2003506.

[38] Y. Liu, A. Yangui, R. Zhang, A. Kiligaridis, E. Moons, F. Gao, O. Inganäs, I. G. Scheblykin, F. Zhang, *Small Methods* **2021**, *5*, 2100585.

[39] Y. Li, X. Huang, K. Ding, H. K. M. Sheriff, L. Ye, H. Liu, C.-Z. Li, H. Ade, S. R. Forrest, *Nat. Commun.* **2021**, *12*, 5419.

[40] K. Jiang, J. Zhang, Z. Peng, F. Lin, S. Wu, Z. Li, Y. Chen, H. Yan, H. Ade, Z. Zhu, A. K. Y. Jen, *Nat. Commun.* **2021**, *12*, 468.

[41] Y. Cui, H. Yao, J. Zhang, K. Xian, T. Zhang, L. Hong, Y. Wang, Y. Xu, K. Ma, C. An, C. He, Z. Wei, F. Gao, J. Hou, *Adv. Mater.* **2020**, *32*, 1908205.

[42] C. Li, J. Zhou, J. Song, J. Xu, H. Zhang, X. Zhang, J. Guo, L. Zhu, D. Wei, G. Han, J. Min, Y. Zhang, Z. Xie, Y. Yi, H. Yan, F. Gao, F. Liu, Y. Sun, *Nat. Energy* **2021**, *6*, 605.

[43] L. Ye, W. Zhao, S. Li, S. Mukherjee, J. H. Carpenter, O. Awartani, X. Jiao, J. Hou, H. Ade, *Adv. Energy Mater.* **2017**, *7*, 1602000.

[44] R. Ma, T. Liu, Z. Luo, K. Gao, K. Chen, G. Zhang, W. Gao, Y. Xiao, T.-K. Lau, Q. Fan, Y. Chen, L.-K. Ma, H. Sun, G. Cai, T. Yang, X. Lu, E. Wang, C. Yang, A. K. Y. Jen, H. Yan, *ACS Energy Lett.* **2020**, *5*, 2711.

[45] M. Sumita, K. Sakata, S. Asai, K. Miyasaka, H. Nakagawa, *Polym. Bull.* **1991**, *25*, 265.

[46] L. Zhan, S. Li, Y. Li, R. Sun, J. Min, Y. Chen, J. Fang, C.-Q. Ma, G. Zhou, H. Zhu, L. Zuo, H. Qiu, S. Yin, H. Chen, *Adv. Energy Mater.* **2022**, 2201076.

[47] Z. Chen, X. Chen, Z. Jia, G. Zhou, J. Xu, Y. Wu, X. Xia, X. Li, X. Zhang, C. Deng, Y. Zhang, X. Lu, W. Liu, C. Zhang, Y. Yang, H. Zhu, *Joule* **2021**, *5*, 1832.

[48] R. Wang, C. Zhang, Q. Li, Z. Zhang, X. Wang, M. Xiao, *J. Am. Chem. Soc.* **2020**, *142*, 12751.

[49] J. Yao, T. Kirchartz, M. S. Vezie, M. A. Faist, W. Gong, Z. He, H. Wu, J. Troughton, T. Watson, D. Bryant, J. Nelson, *Phys. Rev. Appl.* **2015**, *4*, 014020.

[50] U. Rau, *Phy. Rev. B* **2007**, *76*, 085303.

[51] X. Xia, T.-K. Lau, X. Guo, Y. Li, M. Qin, K. Liu, Z. Chen, X. Zhan, Y. Xiao, P. F. Chan, H. Liu, L. Xu, G. Cai, N. Li, H. Zhu, G. Li, Y. Zhu, T. Zhu, X. Zhan, X.-L. Wang, X. Lu, *Nat. Commun.* **2021**, *12*, 6226.

[52] T. P. Chaney, A. J. Levin, S. A. Schneider, M. F. Toney, *Mater. Horiz.* **2022**, *9*, 43.

[53] D.-M. Smilgies, *J Appl. Cryst.* **2009**, *42*, 1030.

[54] S. Liu, J. Yuan, W. Deng, M. Luo, Y. Xie, Q. Liang, Y. Zou, Z. He, H. Wu, Y. Cao, *Nat. Photonics* **2020**, *14*, 300.